Fe_3O_4 Nanoparticles Embedded in Uniform Mesoporous Carbon Spheres for Superior High-Rate Battery Applications

*Yu Chen, Bohang Song, Meng Li, Li Lu, and Junmin Xue**

Robust composite structures consisting of Fe_3O_4 nanoparticles (~5 nm) embedded in mesoporous carbon spheres with an average size of about 70 nm (IONP@mC) are synthesized by a facile two-step method: uniform Fe_3O_4 nanoparticles are first synthesized, followed by a post-synthetic low-temperature hydrothermal step to encapsulate them in mesoporous carbon spheres. Instead of graphene, which has been extensively reported for use in high-rate battery applications as a carbonaceous material combined with metal oxides, mesoporous carbon is chosen to enhance the overall performances. The interconnecting pores facilitate the penetration of electrolyte, leading to direct contact between electrochemically active Fe_3O_4 and lithium ion-carrying electrolyte, greatly facilitating lithium ion transportation. The interconnecting carbon framework provides continuous 3D electron transportation routes. The anodes fabricated from IONP@mC are cycled under high current densities ranging from 500 to 10 000 mA g^{-1}. A high reversible capacity of 271 mAh g^{-1} is reached at 10 000 mAh g^{-1}, demonstrating its superior high rate performance.

1. Introduction

To develop the next generation Lithium Ion Batteries (LIBs) for the application of electric vehicles, many critical issues must be addressed, such as energy density/power density and cycling stability. From the aspect of anode materials for LIBs, despite the great effort that has been put in boosting the overall energy density by applying new anode materials, such as metal oxides,[2] metal sulfides,[3] and lithium alloying metals (Si,[4] Ge,[5] Sn,[6] the main obstacle in reaching a LIB with overall satisfactory performance lies in the poor performances in power density and cycling stability.[7] In order to build an anode material with high power density and long cyclic stability, a specially designed heterogeneous structure is required. Each component of such heterogeneous structure should be tailored to address a specific problem. Mesoporous structure has been proven to be beneficial for the LIB application. In literature, zhou and his co-workers have synthesized electrodes consisting mesoporous metal oxides and carbon coating with superior lithium storage performances. Besides, mesoporous carbon is considered as an ideal framework to encapsulate electrochemically active particles for LIB applications.[11] The ordered mesopores provide confined spaces for the accommodation of electrochemically active particles, where the volume expansion of these particles can be buffered by mesopores and carbon matrix; while the interlaced networks of interconnecting pores and carbon framework provide perfect channels for electrolyte penetration and electron conduction, respectively.[12]

In this work, with the aim at reaching high power density and satisfactory cyclic stability, composite anode materials composed of iron oxide (Fe_3O_4) nanoparticles with diameter around 5 nm confined inside mesoporous carbon spheres with uniform size (~70 nm) were synthesized. Iron oxide (Fe_3O_4) was chosen as the electrochemical active component in such composite, due to its high theoretical capacity,[13] ease of fabrication into nanosize,[14] and compatibility with the overall synthesis. To boost the power density of an anode material, nano-sized Fe_3O_4 particles are preferred due to their significant shorter lithium path length compared with their bulk counterpart.[15] Besides, the small size is able to partially buffer the stress and strain related to the particle volume expansion/contraction during the lithium insertion/removal.[16] Furthermore, the resultant high surface area permits a higher contact area between electrolyte and electrode, thus achieving a higher lithium flux across the interface.[17] Being embedded in mesoporous carbon sphere, these nano-sized Fe_3O_4 particles were in direct contact with both lithium ion and electron transportation media, namely electrolyte and carbon, which was beneficial for high rate performances. Also, the volume change of Fe_3O_4 nanoparticles was greatly buffered by the mesopores and surrounding carbon matrix. Each Fe_3O_4 nanoparticle was held in position by the carbon matrix, preventing them from agglomeration upon cycling. Moreover, the 3-D carbon spheres provides the robustness which was necessary to maintain the

---

Y. Chen, M. Li, Dr. J. Xue
Department of Materials Science and Engineering
National University of Singapore
Singapore, 117576
E-mail: msexuejm@nus.edu.sg
B. Song, Prof. L. Lu
Department of Mechanical Engineering
National University of Singapore
Singapore, 117576

DOI: 10.1002/adfm.201300872

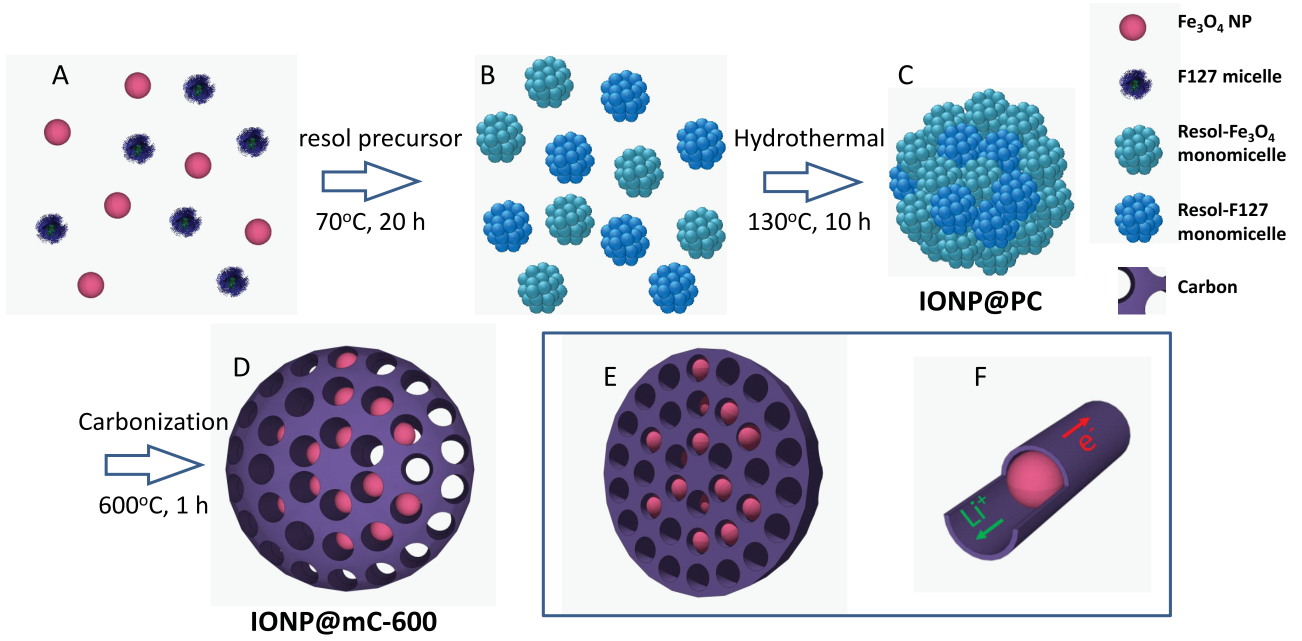

Figure 1. Schematic representation of the formation of IONP@mC-600. (A) IONPs and F127 micelles, (B) resol-Fe$_3$O$_4$ and resol-F127 monomicelles, (C) IONP@PC, (D) IONP@mC, (E) cross section of IONP@mC, and (F) magnified representation of a channel of IONP@mC.

structure integrity, as well as the cyclic stability of such anode composite.[18] Compared with the commonly reported graphene in metal oxide composite electrodes, mesoporous carbon has several advantages: relative ease in synthesis via a low temperature hydrothermal method,[19] large quantity can be obtained after every hydrothermal process,[20] and a much safer fabrication process that does not include highly concentrated acids.

In literature, there are several works reporting the incorporation of electrochemically active nanoparitcles into mesoporous carbon network. Kang and co-workers synthesized Fe$_3$O$_4$ nanocrystals confined in mesocellular carbon foam with irregular macropores via a host-guest approach for LIB application.[21] Wu and co-workers reported an ammonia-atmosphere pre-hydrolysis post-synthetic route for ordered mesoporous carbon encapsulating iron oxide (Fe$_2$O$_3$) for arsenic removal.[22] Fan et al. also prepared a tin oxide/mesoporous cabon composite by deposition of tin chloride and phosphorus ester into mesoporous carbon for LIB anode application.[11] For all these aforementioned works, porous carbon frameworks were firstly synthesized and metal oxide particles were encapsulated via a post treatment, in which metal precursors were dissolved in porous-carbon-containing media and turned into oxides via hydrolysis followed by pyrolysis. However, such process led to unavoidable condensation of metal oxide particles on the surface of porous carbon, where the merits of utilizing porous framework cannot be realized. In this work, the key concept is to synthesize iron oxide nanoparticles (IONPs) first, followed by a post treatment to make sure all of these IONPs were encapsulated in mesoporous carbon spheres. The schematic presentation of such synthesis method is shown in **Figure 1**. First, ultra-small water-soluble IONPs coated by dehydro-ascorbic acid (DHAA) were synthesized via a hydrothermal method with L-ascorbic acid used as surfactant.[14] The morphological characterization of these IONPs was shown in Figure S1. As-synthesized IONPs were dispersed in the aqueous solution of triblock Pluronic F127 where they formed micelles due to their amphiphilic nature (Figure 1A). With the addition of phenolic resol, spherical resol-F127 and resol-Fe$_3$O$_4$ monomicelles were formed via the hydrogen bond interaction between resol and F127/DHAA (Figure 1B).[20] During the subsequent low-concentration hydrothermal treatment, these two kinds of monomicelles further assembled into spherical resol composite, forming iron oxide nanoparticles encapsulated in polymeric composite (IONP@PC) as shown in Figure 1C. Finally, iron oxide nanoparticles embeded in mesoporous carbon (IONP@mC) spheres were obtained after a high temperature treatment in an inert atmosphere where carbon framework and accessible mesopores were generated by the carbonization of phenolic resol and the removal of triblock F127, respectively (Figure 1D). Two different carbonization temperatures (450 °C and 600 °C) were used to give the final products: IONP@mC-450 and IONP@mC-600, respectively. Through such synthesis method, all Fe$_3$O$_4$ nanoparticles were encapsulated inside of carbon beads because they were trapped in resol-Fe$_3$O$_4$ monomicelles at the early stage of reaction (Figure 1B). Figure 1E and F show the schematic illustrations of the cross-section and electron/lithium transportation channels of IONP@mC, respectively.

2. Results and Discussion

The morphologies of IONP@PC and IONP@mC-600 were examined by transmission electron microscopy (TEM) and are shown in **Figure 2**. IONP@mC-450 were also examined under TEM (Figure S2) and showed similar morphology to IONP@mC-600. Figure 2A and C show the morphology of

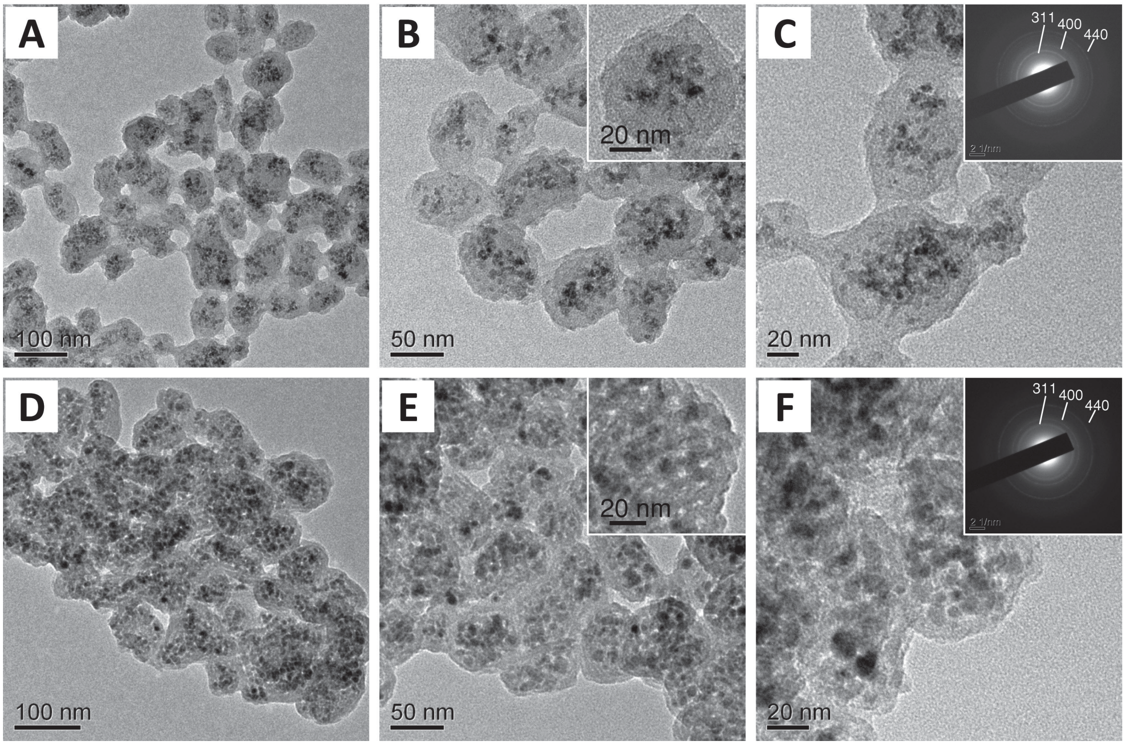

Figure 2. TEM images of IONP@PC (A-C) and IONP@mC-600 (D-F). Insets of B and D: magnified TEM images of one IONP@PC and IONP@mC-600. Insets of C and F: SAED patterns of IONP@PC and IONP@mC-600.

IONP@PC and IONP@mC-600 under low magnification, respectively. Both of them were in spherical or elliptical shapes. The average sizes of these two spheres were measured and calculated to be 75.1 and 71.6 nm, respectively, with the size distribution graphs are shown in Figure S3. The reduction in average size after carbonization is due to the slight shrinkage of polymeric spheres after the removal of F127 template and carbonization of polymeric composite.[23] Under higher magnifications, lots of distinct IONPs could be observed within each IONP@PC and IONP@mC-600 as shown in Figure 2B and E, indicating the successful incorporation of IONPs. Besides, compared with IONP@PC as shown in Figure 2B, numerous white dots can be observed in IONP@mC-60 as shown in Figure 2E, representing mesopores generated by the removal of the soft template F127. By comparing the magnified IONP@PC and IONP@mC-600 shown in the Insets of Figure 2B and E, both mesopores and IONPs could be clearly observed in IONP@mC-600. Under the highest magnification TEM images as shown in Figure 2C and F, most of IONPs were still very small in size even after a high temperature carbonization treatment. The Insets of Figure 2C and F showed the selected area electron diffraction (SAED) patterns of IONP@PC and IONP@mC-600, respectively. Each distinct diffraction ring was indexed to respective crystal planes for magnetite structure (JCPDS 65–3107). By varying the initial IONPs amount, IONP@mC-600 with different Fe_3O_4 percentages were obtained, with their morphologies showing in Figure S4. Specifically, mesoporous carbon spheres without the incorporation of IONPs were denoted as mC-600.

The X-ray diffraction (XRD) patterns of IONP@PC (black) and IONP@mC-600 (red) were shown in **Figure 3**. The low, broaden diffraction hump around 22° that could be observed for both samples were originated from the carbon matrix.[24] All other diffraction peaks were assigned to cubic magnetite structure (JCPDS 65–3107), which were also consistent with the SAED results. By Sherrer's equation, the average crystal sizes was calculated to be 5.3 and 5.4 nm for IONP@PC and IONP@mC-600, respectively.

Nitrogen sorption isotherms and corresponding pore size distribution curves of pure mesoporous carbon carbonized at

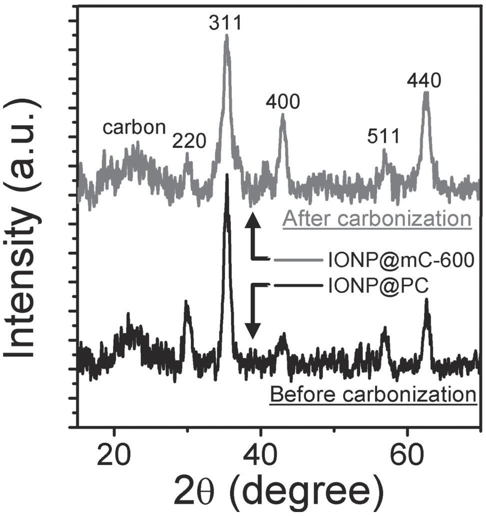

Figure 3. XRD patterns of IONP@PC (lower line) and IONP@mC-600 (upper line).

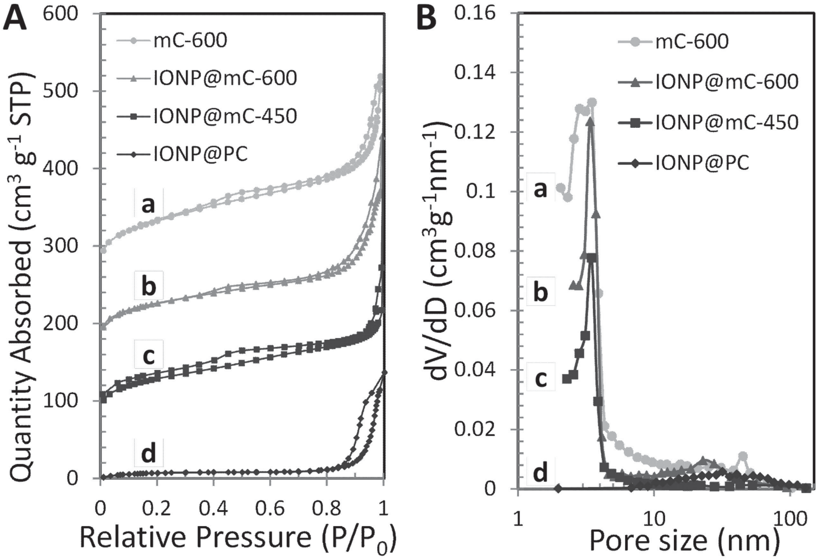

C

	Fe_3O_4 [wt%]	BET surface area [m^{2}g^{-1}] (e)	Pore size [nm] (f)	Pore volume [cm^{3}g^{-1}] (g)
(a) mC-600	-	942.2	4.1	0.767
(b) IONP@mC-600	39.4	699.1	3.4	0.434
(c) IONP@mC-450	32.6	461.6	3.7	0.272
(d) IONP@PC	12.2	40.9	16.2	0.177

Figure 4. (A) Nitrogen sorption isotherms, (B) corresponding pore size distribution curves, and (C) Structural and textual properties of (a) mC-600, (b) IONP@mC-600, (c) IONP@mC-450, and (d) IONP@PC.

600 °C (mC-600), IONP@mC carbonized at 600 °C (IONP@mC-600), IONP@mC carbonized at 450 °C (IONP@mC-450), and IONP@PC were shown in **Figure 4**A and B. Their porous characteristics and corresponding Fe_3O_4 percentage were summarized in Figure 4C. The nitrogen sorption isotherms of carbonized samples, namely mC-600, IONP@mC-600, and IONP@mC-450, showed combined type I/IV sorption isotherms with BET surface areas of 942.2, 699.1, and 461.6 m^2 g^{-1}, respectively. Hysteresis loops at both high and low pressures could be observed for all of these three samples. Such behavior indicated all these three spheres have both micropores and mesopores, where the micopores corresponded to the interparticle texture between spheres and mesopores were formed by removing the soft template, triblock F127, after carbonization process, respectively.[19,20,25] Prior to carbonization, no mesopores existed in IONP@PC and the hysteresis loop at high pressure could be observed. The pore sizes of these four samples were derived from the Barrett–Joyner–Halenda (BJH) model from the desorption branches of the isotherms to be 4.1, 3.4, 3.7, and 16.2 nm for mC-600, IONP@mC-600, IONP@mC-450, and IONP@PC, respectively. These values were consistent with those can be observed from TEM images shown in Figure 2 and S2. The pore volumes of these four samples were also presented in Figure 4C. Compared with the pristine mesoporous carbon (mC-600), samples with IONPs embedded (IONP@mC-600 and IONP@mC-450) showed lower surface areas and pore volumes, which could be originated from the increment in overall density by introducing IONPs. As summarized in Figure 4C, both the surface areas and pore volumes of the carbonized samples (IONP@mC-600 and IONP@mC-450) were much higher than those of IONP@PC. Such porous structures were desired for the penetration of electrolyte and the accommodation of volume change of IONPs, which were beneficial to the resultant battery performances. Furthermore, these samples were examined by thermogravimetric analysis (TGA) (Figure S5), with a high IONPs percentage of 39.4 wt% for IONP@mC-600.

Figure 5 showed the X-ray photoelectron spectroscopy (XPS) spectrum of IONP@PC (Figure 5A) and IONP@mC-600 (Figure 5C) carried out in the region of 200–800 eV with the high resolution spectrum of C1s shown in Figure 5B and D, respectively. As shown in Figure 5A, there was no Fe2p signal observed, indicating that all IONPs were successfully embedded in polymeric sphere. Similarly, the Fe2p peak was very weak after carbonization. Besides, a huge reduction in O1s intensity was observed after carbonization, showing the successful carbonization process. Furthermore, the corresponding high resolution C1s XPS spectrum of IONP@PC and IONP@mC-600 shown in Figure 5B

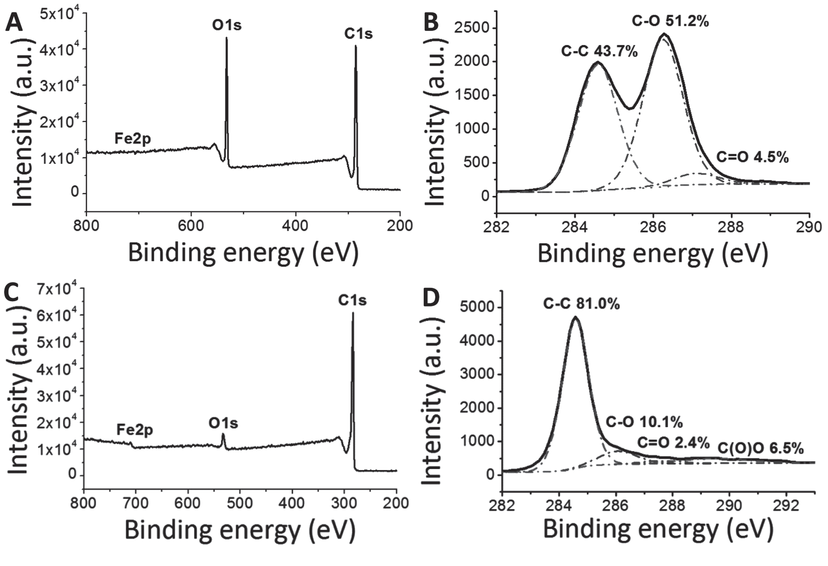

Figure 5. XPS spectrum of (A) IONP@PC and (C) IONP@mC-600. High resolution XPS spectrum of C1s from (B) IONP@PC and (D) IONP@mC-600.

and D were deconvoluted into four peaks: sp^2 bonded carbon (C-C), epoxy/hydroxyls (C-O), carbonyls (C = O), and carboxyls (O-C = O). As shown in the figure, after carbonization process, the relative carbon content of sp^2 bonded carbon at 286.4 eV increased from 43.7 to 81.0% from IONP@PC to IONP@mC-600. The XPS and high resolution C1s XPS spectrum from IONP@mC-450 were shown in Figure S6, with sp^2 bonded carbon having a relative carbon content of 56.2%.

The electrochemical performances of IONP@mC-600 (carbonized at 600 °C), IONP@mC-450 (carbonized at 450 °C), IONP@PC (without carbonization) were examined using CR2016 coin-cells with lithium metal as counter electrode. The electrode fabricated using IONP@mC-600 as active material was firstly tested at a current density of 500 mA g^{-1}. **Figure 6**A shows the charge/discharge profiles of IONP@mC-600 at the first three cycles from 3 to 0.005 V. A plateau around 0.8 V versus Li^+/Li^0 in the first discharge curve was observed, corresponding to the reduction of Fe_3O_4 to Fe^0 in conversion reaction: $Fe_3O_4 + 8e^- + 8Li^+ \rightarrow Fe^0 + 4Li_2O$.[21] A sloping plateau around 1.8 V in the first charge profile reflected the reverse reaction.[26] The discharge and charge capacities in the first cycle were 1214.3 and 711.6 mAh g^{-1}, respectively, with a first cycle capacity loss of 41%. High initial capacity loss is commonly observed for oxide anode materials.[27] Besides, the large surface area of the as-obtained mesoporous structure promoted the formation of solid electrolyte interface (SEI), which also contributed to the capacity loss in the first cycle.[28] In the second cycle, IONP@mC-600 delivered discharge and charge capacities of 734.2 and 671.2 mAh g^{-1}, with the coulombic efficiency of 91.4%. In order to demonstrate its high rate performance, IONP@mC-600 was tested under a wide range of current densities up to 10 000 mA g^{-1}. Figure 6B showed the charge/discharge profiles of IONP@mC-600 of the last cycles at different current densities.

The cell fabricated from IONP@mC-600 was firstly investigated under a rate capability test from 500 to 2000 mA g^{-1}. As shown in Figure 6C, during the first 20 cycles under the current density of 500 mA g^{-1}, the reversible capacity of IONP@mC slowly stabilized to around 580 mA g^{-1}, with the charge capacity at 20th cycle being 576.5 mAh g^{-1}. Meanwhile, the coulombic efficiency rose from 58.6% at the first cycle to above 98% at last several cycles, indicating stabilization of SEI. The cell

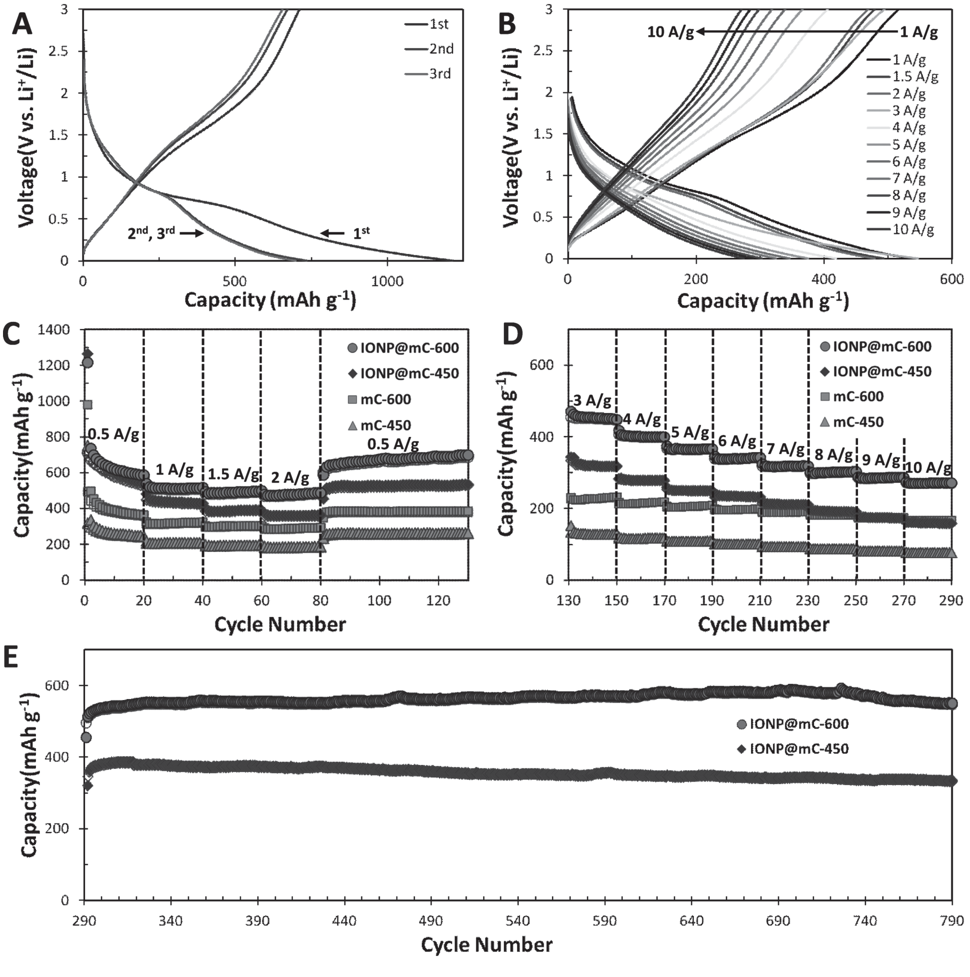

Figure 6. Electrochemical performances of IONP@mC-600, IONP@mC-450, and IONP@PC. Charge/discharge profiles of IONP@mC-600 at (A) current densities of 500 mA g^{-1} and (B) higher rates from 1000 to 10 000 mA g^{-1}. Rate capability tests of IONP@mC-600 (sphere), IONP@mC-450 (diamond), mC-600 (square), and mC-450 (triangle) (C) from 500 to 2000 mA g^{-1}, and (D) from 3000 to 10 000 mA g^{-1}. (E) Subsequent cycling tests of IONP@mC-600 and IONP@mC-450 at 2000 mA g^{-1} for 500 cycles.

was then subjected to higher current densities of 1000, 1500, and 2000 mAg^{-1}. As shown in Figure 6C, IONP@mC-600 showed excellent cyclic stability and delivered 517.2, 497.5, and 487.9 mAh g^{-1} at the 20th cycles of 1000, 1500, and 2000 mA g^{-1}, respectively. More importantly, the coulombic efficiencies at these stages were very close to 100%, indicating the facile transportation of lithium ion and electron, provided by the interlaced carbon framework and mesopores. After the current density being reduced to 500 mA g^{-1}, the reversible capacity restored to above 630 mAh g^{-1}, and slowly increased to 697.4 mAh g^{-1} at the overall 130th cycle, demonstrating its excellent cell stability. For comparison, cells fabricated from IONP@mC-450, mC-600, and mC-450 were also tested under the same condition. As shown in Figure 6C, IONP@mC-450 (red diamond) showed similar cyclic behavior as that of IONP@mC-600 with a quite stable cyclic performance. With a higher content of oxygen-containing groups due to the lower carbonization temperature, the first discharge capacity of IONP@mC-450 was slightly higher than that of IONP@mC-600, caused by the reaction between lithium and oxygen-containing functional groups. After stabilization, IONP@mC-450 showed lower reversible capacities as compared to those of IONP@mC-600.

To further demonstrate its advantage for high rate LIB application, the rate performance of IONP@mC-600 was further tested under higher current densities from 3000 to 10 000 mA g^{-1}. As shown in figure 6D, the capacities of IONP@mC-600 (blue spheres) under all current densities were quite stable, showing superior rate capability. Specifically, the last reversible capacities of IONP@mC-600 were 447.1, 398.9, 365.8, 342.0, 318.9, 302.8, 287.2, and 271.1 mAh g^{-1} at the 20th cycles of 3000, 4000, 5000, 6000, 7000, 8000, 9000, and 10 000 mA g^{-1}, respectively. Few works have reported the battery performances of iron oxide-based anodes under the current density of 10 000 mA g^{-1}. Behera has synthesized Fe_3O_4-graphene by an ultrasonic assisted co-precipitation technique with a reversible capacity of 180 mAh g^{-1} at 10 000 mA g^{-1}.[29] Zhang and co-workers also reported the post-pyrolysis RGO-Fe_3O_4 nanocomposite having a reversible capacity of 192 mAh g^{-1} under the current density of 9260 mA g^{-1}.[30] At the current density of 10 000 mA g^{-1}, the capacity of IONP@mC-600 is at least 40% higher than these two reported values, indicating its superior performance under high current densities. Graphene is usually chosen as the supplementary component when combining with metal oxides for high rate LIB application.[29] Figure S7 showed the comparison between of the high rate performances between IONP@mC-600 in this work and reported Fe_3O_4/graphene composites at current densities above 1000 mA g^{-1}. Compared with others, IONP@mC-600 showed a more stable high rate performance with the minimum decrease in capacity as current density increases. Besides, the reversible capacities of IONP@mC were higher than those of reported Fe_3O_4/graphene composites when the current density was above 5000 mA g^{-1}. Furthermore, IONP@mC-450 (red diamond) was also tested under the same rate capability test ranging from 3000 to 10 000 mA g^{-1}, with a reversible capacity of 158.9 mAh g^{-1} at the last cycle under 10 000 mA g^{-1}. Without the embedment of Fe_3O_4 nanoparticles, the first reversible capacity for mC-600 and mC-450 (pristine mesoporous carbon spheres calcinated at 450 °C) were 492 and 319 mAh g^{-1} under the current density of 500 mA g^{-1}, respectively. As the current density increased, the reversible capacities of mC-600 and mC-450 were still much worse comparing with their counterparts with the incorporation of Fe_3O_4 nanoparticles, namely IONP@mC-600 and IONP@mC-450, indicating the crucial contribution of Fe_3O_4 content in the overall capacities even under high current densities (3000 to 10 000 mA g^{-1}). Specifically, under the current density of 10 000 mA g^{-1}, with the incorporation of Fe_3O_4 nanoparticles, the reversible capacities of IONP@mC-600 was 271 mAh g^{-1}, which was 103 mAh g^{-1} higher than that of mC-600. Taking the individual capacities of IONP and carbon to be 922 and 492 mAh g^{-1}, based on TGA results (Figure S5), the theoretical capacity of IONP@mC-600 is 662 mAh g^{-1}. Such value is consistent with the stabilized reversible capacities obtained during cycle 80 to 130 at the current density of 500 mA g^{-1}. However, this theoretical value is lower than the first reversible capacity of IONP@mC-600 (712 mAh g^{-1}) and those of several subsequent cycles. The extra capacities observed can be attributed to the reversible formation and dissolution SEI components, including various inorganic and organic compounds. Besides, metal nanoparticles (Fe) formed during discharge have been reported to perform as efficient catalysts to promote such reversible process, improving the overall capacities. Such phenomenon of SEI components providing extra capacities has been well documented in literature.

The morphological design of IONP@mC in this work played a crucial role in its satisfactory high rate performances. Desirable structure features, such as mesoporous carbon, ultrasmall size of Fe_3O_4, and finely embedment of Fe_3O_4 within the carbon matrix, are beneficial for the battery performance under high current density. Specifically, either electron pathway or lithium ion pathway can be the limiting factor for the high rate performance of an electrode material. For the IONP@mC in this work, the mesoporous carbon frameworks provide high speed electron transportation channels; while the mesopores provided by such carbon structure are easily penetrated by the lithium ion carrying electrolyte, providing high speed channel for lithium ion transportation. In this way, both high speed electron and lithium ion pathways are provided. More importantly, the electrochemically active Fe_3O_4 nanoparticles possess very small sizes, with an average size of 5.4 nm. Such small dimensions provide very short lithium ion diffusion lengths (L) within these particles, thus significantly reducing the characteristic time constant t for the lithium ion diffusion process, which is proportional to L^2 (($t = L^2/D$, where D is the diffusion constant). Therefore, due to the small sizes of Fe_3O_4 particles, the rate of lithium ions insertion/removal is significantly enhanced, which is crucial to the satisfactory high rate performance of IONP@mC electrodes.

The superior cyclic stability of IONP@mC-600 anode material was further demonstrated by testing the same cell under 2000 mA g^{-1} for 500 cycles. As shown in Figure 6E, after being cycled at various high current densities up to 10 000 mA g^{-1}, the reversible capacity of IONP@mC-600 restored to 510 mAh g^{-1} at the first cycle, which was already higher than the previous capacity obtained under the same rate (Figure 6C). Subsequently, the reversible capacity quickly increased to above 530 mAh g^{-1} after 6 cycles and stabilized around 560 mAh g^{-1} during the subsequent cycles. At the 500th cycle under the current density of 2000 mA g^{-1}, which is also the overall 790th cycle, such anode fabricated from IONP@mC-600 was able to deliver a reversible capacity of 547.8 mAh g^{-1}. The anode of IONP@mC-450 was also further cycled at 2000 mA g^{-1} for 500 cycles, showing inferior performance with a reversible capacity of 332.5 mAh g^{-1} at the last cycle.

IONP@mC-600 with a higher Fe_3O_4 content (~65.5%) was also synthesized through the same procedure by adding more IONP during polymeric composite formation. However, as shown in Figure S8A and S8B, the desired morphologies presented in Figure 2A–C (Fe_3O_4 nanoparticles embedded in spherical polymeric nanobeads) were lost when a higher amount of Fe_3O_4 nanopartices were used in the synthesis. After calcination, without enough surface protection from carbon framework, the Fe_3O_4 particles grew into much bigger sizes (Figure S8C and S8D), which are undesirable for high rate battery applications. As shown in Figure S9A, under comparatively low current densities, IONP@mC-600 with higher IONP content delivered higher reversible capacities due to its higher Fe_3O_4 content. However, as the current density increased beyond 3000 mA g^{-1}, due to the large Fe_3O_4 nanoparticle size, IONP@mC-600 with higher IONP content showed much worse electrochemical performance (Figure S9B).

Higher calcination temperatures, 750 °C and 900 °C, were also performed on the as-synthesized IONP@PC to obtain IONP@mC-750 and IONP@mC-900, respectively. As indicated by their C1s peaks shown in Figure S10A and S10B, more complete carbonizations were achieved under higher calcination temperatures. However, the Fe_3O_4 nanoparticles sizes of these two samples increased significantly. Besides, the spherical structure and ordered mesoporous carbon framework were lost under such high carbonization temperatures. The significant growth the Fe_3O_4 particle size can have detrimental effect on the electrochemical performance of IONP@mC, especially under high current densities. As shown in Figure S11, under exact same test condition as IONP@mC-450, IONP@mC-750 and IONP@mC-900 showed much inferior performances. Specifically, the reversible capacities of IONP@mC-750 and IONP@mC-900 were 94 and 59 mAh g^{-1} at the current density of 10 000 mA g^{-1}, respectively. These values are much lower than the reversible capacity of IONP@mC-600 (271 mAh g^{-1}) at the same current density. Furthermore, under high calcinations temperatures (750 °C and 900 °C), the surface of Fe_3O_4 nanoparticles can be partially reduced to Fe.[22] Under the examination of SAED of USIO@mC-750 and 900 shown in Figure S12, (200) diffraction dots from Fe (JCPDS 89–4185) were observed. The formation of Fe can further reduce the reversible capacity of the composites.

The morphologies of IONP@mC-600 beads after 790 charge/discharge cycles with current density up to 10 000 mA g^{-1} are shown in Figure S13. Figure S13A and S13B show the SEM images of cycled IONP@mC-600 beads under two different magnifications. As shown, the cycled IONP@mC-600 beads still possessed spherical shapes, showing their good structure integrities. TEM images were used to exam the state of the embedded Fe_3O_4 nanoparticles. Figure S13C shows the typical morphology of a cycle IONP@mC-600 bead. The dark dots represent the Fe_3O_4 nanoparticles. Under a closer examination (Figure S13D), although each dark dot seems to be around 10 nm (larger than their sizes before cycle), each dot actually is consisted of several smaller particles, demonstrating the Fe_3O_4 particles still possess very small sizes after such a harsh cycling process. The prepared electrode consisting of active material (IONP@mC-600), carbon black (Super P) and Polyvinylidene Fluoride (PVDF) was examined by XRD (Figure S14). As shown in Figure S14A, several main peaks of cubic Fe_3O_4 (JCPDS 65–3107) were observed. However, after 1 cycle of charge/discharge, these peaks became very weak and were very difficult to be observed. The possible reason for this is that the Fe_3O_4 crystal structure might be damaged in the charge/discharge process due to the volume expansion. Such phenomenon is also well documented in literature.[13] Figure S14B shows the XRD pattern of IONP@mC-600 after 790 cycles up to the current density of 10 000 mA g^{-1}. As expected, the peaks from Fe_3O_4 cannot be observed. All peaks shown in Figure S14B can be ascribed to Li_2CO_3 and LiF, which formed during the charge/discharge process.

3. Conclusions

Nano-sized electrochemically active Fe_3O_4 (~5 nm) embedded in mesoporous carbon beads composite beads (IONP@mC) were fabricated by a carefully designed synthetic route. The obtained composites possess desired structure for high rate battery applications: (1) The volume expansion/contraction of Fe_3O_4 was buffered by surrounding mesopores and carbon matrix; (2) the ultrasmall size of Fe_3O_4 also partially buffer its volume change and hugely reduce the lithium ion transportation path; (3) the 3D interlaced mesopores and carbon frameworks provide excellent routes for lithium ion and electron, respectively; (4) the mesoporous carbon beads provide the robustness which is crucial to prevent the structural failure of the anode. Therefore, the obtained IONP@mC composites delivered stable capacities under various high current densities. Even compared with Fe_3O_4-based composites with graphene incorporated, IONP@mC shows much more stable capacity as current density increases. Besides, the capacities of INOP@mC-600 are higher than those of Fe_3O4/graphene composites under current densities (above 5000 mA g^{-1}). Specifically, a reversible capacity of 271.1 mAh g^{-1} was reached by IONP@mC-600 even at the current density of 10 000 mA g^{-1}, demonstrating its great potential of being utilized as the anode material in high rate battery application.

4. Experimental Section

Synthesis of Water-Soluble Fe_3O_4 Nanoparitlces: The synthesis method was reported by Mathur and co-workers.[14] In a typical synthesis, $FeCl_3 \cdot 6H_2O$ (0.8109 g) and $NaHCO_3$ (0.756 g) were dissolved in deionized water (30 mL) with the aid of magnetic stirring. Meanwhile, L-ascorbic acid (0.088 g) was separately dissolved in deionized water (10 mL) by stirring. After 30 min, two solutions were mixed together and allowed the stirring continue for another 20 min. Finally, the solution was transferred into a 125 mL steel-lined Teflon autoclave and treated hydrothermally at 150 °C for 6 h. The as-obtained particles were collected by centrifuge and washed by ethanol followed by de-ionized water for several times.

Synthesis of Iron Oxide Nanoparticles Embedded in Polymeric Composite: In a typical synthesis of IONP@PC, phenol (0.8 g), NaOH (0.1 M, 20 mL) aqueous solution, and formalin (2.8 mL) solution were mixed and stirred at 70 °C for 30 min. Subsequently, deionized water (15 mL) containing well-dissolved triblock Pluronic F127 (1.28 g) and appropriate amount of DHAA-coated Fe_3O_4 nanoparticles were added. After 2 h, deionized water (50 mL) was added and the reaction was allowed for another 20 h. The mixture was diluted 4 times and treated hydrothermally at 130 °C for 10 h to obtain IONP@PC. The obtained brownish sample was washed with ethanol and deionized water for several times. Different sets of samples were obtained by adding different amount of DHAA-coated Fe_3O_4 nanoparticles. For comparison, pristine polymeric composite (PC) was also prepared without adding any IONPs.

Synthesis of Iron Oxide Nanoparticles Embededd in Mesoporous Carbon: The obtained IONP@PC was freeze-dried and transferred into a quartz tube furnace, where it was heat-treated in Ar atmosphere to 450 and 600 °C at 5 °C min^{-1} for 1 h to obtain IONP@mC-450 and IONP@mC-600, respectively. For pure PC, same heat treatments to 450 and 600 °C were applied and pristine mesoporous carbon spheres (mC-450 and mC-600) were obtained.

Materials Characterization: Transmission electron microscopy (TEM) images and selected area electron diffraction (SAED) patterns were collected on a JEOL 100CX instrument, using a 300 kV accelerating voltage. Powder X-ray diffraction (XRD) pattern was measured by a powder diffractometer (Bruker D8 Advanced Diffractometer System) with Cu Kα (1.5418 A) source. Nitrogen sorption isotherms were measured on the Surface Area and Porosity Analyzer (ASAP 2020). X-ray photoelectron spectroscopy (XPS) data were obtained by an Axis Ultra DLD X-ray photoelectron spectrometer equipped with an Al Ka X-ray source (1486.6 eV). The thermogravimetric analysis (TGA) was performed under an air flow of 100 mL min^{-1} using Du Pont Instruments TGA 2950 from room temperature to 1000 °C with a heating rate of 10 °C min^{-1}.

Electrochemical Measurements: The electrochemical cycling tests were performed using CR2016 coin-type cells. A typical cell includes an as-prepared electrode including active material as a working electrode, pure Li foil as a counter electrode, separator (Celgard 2500) and electrolyte (1 M LiPF6 in EC: DEC: DMC = 1:1:1 organic solutions). All the battery cells were assembled in argon-filled glovebox. And all the cycling tests were conducted in a same voltage window of 0.005–3.0 V vs. Li^0/Li^+ at room temperature while various current densities were applied. The working electrode was prepared by mixing active material, carbon black (Super P) and polyvinylidene fluoride (PVDF) in the weight ratio of 70:15:15 in n-methyl-2-pyrrolidone (NMP) solution. Then the obtained slurry was pasted onto a copper foil followed by drying it in a vacuum condition at 120 °C for 12 h before usage. The typical coating thickness was around 18 μm.

Supporting Information

Supporting Information is available from the Wiley Online Library or from the author.

Received: March 11, 2013
Revised: June 14, 2013

---

[1] a) J. M. Tarascon, M. Armand, *Nature* **2001**, *414*, 359; b) M. Armand, J. M. Tarascon, *Nature* **2008**, *451*, 652.
[2] H. Kim, D.-H. Seo, H. Kim, I. Park, J. Hong, K.-Y. Park, K. Kang, *Chem. Mater.* **2012**, *24*, 720.
[3] W. Zhou, Z. Yin, Y. Du, X. Huang, Z. Zeng, Z. Fan, H. Liu, J. Wang, H. Zhang, *Small* **2013**, *9*, 140.
[4] J. K. Yoo, J. Kim, Y. S. Jung, K. Kang, *Adv. Mater.* **2012**, *24*, 5452.
[5] K. H. Seng, M.-h. Park, Z. P. Guo, H. K. Liu, J. Cho, *Nano Lett.* **2013**, *13*, 1230.
[6] Y. J. Hong, M. Y. Son, Y. C. Kang, *Adv. Mater.* **2013**, *25*, 2279.
[7] J. Jiang, Y. Li, J. Liu, X. Huang, C. Yuan, X. W. Lou, *Adv. Mater.* **2012**, *24*, 5166.
[8] a) R. Liu, J. Duay, S. B. Lee, *Chem. Commun.* **2011**, *47*, 1384; b) L. Su, Y. Jing, Z. Zhou, *Nanoscale* **2011**, *3*, 3967; c) Y. Wang, H. Li, P. He, E. Hosono, H. Zhou, *Nanoscale* **2010**, *2*, 1294.
[9] a) S. Yuan, Z. Zhou, G. Li, *Cryst. Eng. Commun.* **2011**, *13*, 4709; b) S. M. Yuan, J. X. Li, L. T. Yang, L. W. Su, L. Liu, Z. Zhou, *ACS Appl. Mater. Interfaces* **2011**, *3*, 705.
[10] a) J. Hwang, S. H. Woo, J. Shim, C. Jo, K. T. Lee, J. Lee, *ACS Nano* **2013**, *7*, 1036; b) I. Grigoriants, L. Sominski, H. Li, I. Ifargan, D. Aurbach, A. Gedanken, *Chem. Commun.* **2005**, *0*, 921.
[11] J. Fan, T. Wang, C. Yu, B. Tu, Z. Jiang, D. Zhao, *Adv. Mater.* **2004**, *16*, 1432.
[12] L. Shen, X. Zhang, E. Uchaker, C. Yuan, G. Cao, *Adv. Energy Mater.* **2012**, *2*, 691.
[13] P. Poizot, S. Laruelle, S. Grugeon, L. Dupont, J. M. Tarascon, *Nature* **2000**, *407*, 496.
[14] L. Xiao, J. Li, D. F. Brougham, E. K. Fox, N. Feliu, A. Bushmelev, A. Schmidt, N. Mertens, F. Kiessling, M. Valldor, B. Fadeel, S. Mathur, *ACS Nano* **2011**, *5*, 6315.
[15] Y. Wang, H. J. Zhang, L. Lu, L. P. Stubbs, C. C. Wong, J. Lin, *ACS Nano* **2010**, *4*, 4753.
[16] Y.-G. Guo, J.-S. Hu, L.-J. Wan, *Adv. Mater.* **2008**, *20*, 2878.
[17] P. G. Bruce, B. Scrosati, J.-M. Tarascon, *Angew. Chem. Int. Ed.* **2008**, *47*, 2930.
[18] J. Gao, M. A. Lowe, H. c. D. Abruña, *Chem. Mater.* **2011**, *23*, 3223.
[19] M. Li, J. Xue, *J. Colloid Interface Sci.* **2012**, *377*, 169.
[20] Y. Fang, D. Gu, Y. Zou, Z. Wu, F. Li, R. Che, Y. Deng, B. Tu, D. Zhao, *Angew. Chem. Int. Ed.* **2010**, *49*, 7987.
[21] E. Kang, Y. S. Jung, A. S. Cavanagh, G.-H. Kim, S. M. George, A. C. Dillon, J. K. Kim, J. Lee, *Adv. Funct. Mater.* **2011**, *21*, 2430.
[22] Z. Wu, W. Li, P. A. Webley, D. Zhao, *Adv. Mater.* **2012**, *24*, 485.
[23] D. Gu, H. Bongard, Y. Meng, K. Miyasaka, O. Terasaki, F. Zhang, Y. Deng, Z. Wu, D. Feng, Y. Fang, B. Tu, F. Schüth, D. Zhao, *Chem. Mater.* **2010**, *22*, 4828.
[24] Y. Meng, G.-H. Wang, S. Bernt, N. Stock, A.-H. Lu, *Chem. Commun.* **2011**, *47*, 10479.
[25] W. Li, F. Zhang, Y. Dou, Z. Wu, H. Liu, X. Qian, D. Gu, Y. Xia, B. Tu, D. Zhao, *Adv. Energy Mater.* **2011**, *1*, 382.
[26] W.-M. Zhang, X.-L. Wu, J.-S. Hu, Y.-G. Guo, L.-J. Wan, *Adv. Funct. Mater.* **2008**, *18*, 3941.
[27] X. Zhu, Y. Zhu, S. Murali, M. D. Stoller, R. S. Ruoff, *ACS Nano* **2011**, *5*, 3333.
[28] G. Zhou, D.-W. Wang, F. Li, L. Zhang, N. Li, Z.-S. Wu, L. Wen, G. Q. Lu, H.-M. Cheng, *Chem. Mater.* **2010**, *22*, 5306.
[29] S. K. Behera, *Chem. Commun.* **2011**, *47*, 10371.
[30] L. Ji, Z. Tan, T. R. Kuykendall, S. Aloni, S. Xun, E. Lin, V. Battaglia, Y. Zhang, *Phys. Chem. Chem. Phys.* **2011**, *13*, 7170.
[31] a) J. Zhou, H. Song, L. Ma, X. Chen, *RSC Adv.* **2011**, *1*, 782; b) X.-C. Chen, W. Wei, W. Lv, F.-Y. Su, Y.-B. He, B. Li, F. Kang, Q.-H. Yang, *Chem. Commun.* **2012**, *48*, 5904; c) S. Yang, Y. Sun, L. Chen, Y. Hernandez, X. Feng, K. Müllen, *Sci. Rep.* **2012**, *2*, 427.
[32] a) L. Zhang, P. Hu, X. Zhao, R. Tian, R. Zou, D. Xia, *J. Mater. Chem.* **2011**, *21*, 18279; b) L. Su, Z. Zhou, P. Shen, *J. Phys. Chem. C* **2012**, *116*, 23974.
[33] a) L. Su, Z. Zhou, P. Shen, *Electrochim. Acta* **2013**, *87*, 180; b) L. Su, Z. Zhou, X. Qin, Q. Tang, D. Wu, P. Shen, *Nano Energy* **2013**, *2*, 276; c) L. Su, Y. Zhong, J. Wei, Z. Zhou, *RSC Adv.* **2013**, *3*, 9035.